Please cite this paper as

Zhu Z, Lu J, and Zhu S (2023) Multi-rate Kalman Filtering for Structural Dynamic Response Reconstruction by Fusing Multi-type sensor Data with Different Sampling Frequencies. Engineering Structures. 293: 116573. https://doi.org/10.1016/j.engstruct.2023.116573

Multi-rate Kalman filtering for structural dynamic response reconstruction by fusing multi-type sensor data with different sampling frequencies

Zimo ZHU, Jubin LU, Songye ZHU*

[a] Department of Civil and Environmental Engineering, The Hong Kong Polytechnic University, Hong Kong, China.

* Corresponding author: Songye Zhu, Email: songye.zhu@polyu.edu.hk

Abstract

In this paper, a novel dynamic response reconstruction method based on multi-rate Kalman filtering (MRKF) is presented. The proposed method starts with representing the structural system by the state-space equation. Then, different observation equations are defined, and that selection is based on the availability of sensor types at a specific time. Not only can the multi-type sensor data sampled at different rates be fused directly, but the presented method also relaxes the collocated monitoring requirement. In addition, future observations are used to benefit the current state estimation by the Rauch, Tung, and Striebel smoothing procedure. The unobserved structural dynamic responses are estimated using the MRKF virtual sensing technique with multi-rate sensor data. Several demonstrative numerical tests are performed to verify the superiority and robustness of the presented MRKF method on one benchmark shear frame model. The experimental test employed a computer-vision-based displacement tracking technique. Results show that the proposed method surmounts the obstacle to deploying consumer-grade cameras in Structural Health Monitoring (SHM) applications, which provide a low-cost sensing solution without sacrificing response estimation accuracies.

Keywords: Structural health monitoring; response reconstruction; virtual sensing; multi-rate Kalman filtering; sensor data fusion; smoothing

1. Introduction

Structural health monitoring (SHM) techniques have flourished and matured over the past decades; and have been successfully deployed in various structures [1-5]. One of the prime objectives of SHM is to record structural responses and provide useful information for structural health condition assessment. For example, accelerations in wide frequency and amplitude ranges can be recorded by accelerometers with a relatively high sampling rate. Dynamic displacements are related to structural deformation, providing direct information on structural condition assessment. Although, theoretically, displacement can be calculated by double integrating acceleration signals, the results are generally unreliable because of errors accumulated during integration. In particular, quasi-static displacement cannot be calculated through this method. Consequently, a comprehensive SHM sensing system is commonly equipped with multi-type sensors to obtain accurate structural responses.

Sensors are typically installed on hotspots to assess structural health conditions efficiently. A densely distributed sensor network will increase the budget and the deployment difficulties. Structural response reconstruction techniques (also known as virtual sensing techniques), which aim to provide full-field structural response estimations through partial sensor observations, have been widely explored in SHM. Early-stage response reconstruction algorithms were performed in the frequency domain, such as the transmissibility-based [6,7]. Recent research efforts have been more dedicated to the time domain methods. Response reconstruction based on empirical mode decomposition (EMD) is one example in the time domain. He et al. [8] presented the EMD method with intermittency criteria and transformation equations derived from a finite element model. The inverse optimization-based method is another method in the time domain, wherein the reconstruction problem is defined as an inverse optimization problem subject to constraints [9]. However, representing complex structures using simple functions is ambiguous, and the computational cost is scarcely affordable for real-world civil structures. More virtual sensing algorithms have been proposed recently, such as the Bayesian method by Kullaa [10] and the multi-resolution analysis by Saltari et al. [11].

Meanwhile, structural response reconstruction algorithms with affordable computational requirements have a promising future. Specifically, Kalman filter (KF) based methods have undergone extensive research. KF proposed in 1960 [12] can provide a least-square unbiased estimation based on noisy observations. KF estimates structural responses through partial observations. A multi-scale KF-based response reconstruction algorithm was presented by Zhu et al. in 2013 [13]. By representing the state space equation in modal coordinates, high vibration modes can be truncated to simplify the calculation [14] and reduce state estimation errors [15] for MDOF structures. Extended KF (EKF) considers the nonlinearities in structural systems and can be regarded as a nonlinear version of KF. Lei et al. [16] presented an adaptive EKF approach to track changes in structural parameters. Furthermore, structural identification and control through partial observation were achieved in tandem by EKF [17]. When the external input is unknown, most current algorithms [18-20] are based on the filters proposed by Gillijns and De Moor [21, 22]. The availability and number of accelerometers determine the rank of the feedthrough matrix in the state-space equation, and a corresponding response reconstruction filter shall be selected according to that ranking.

Current response reconstruction algorithms usually need multi-type sensors to guarantee state estimation accuracy. The direct fusion of different types of sensors may be challenging. Zhang et al. [23, 24] solved the matrix illness problem encountered during multi-type sensor data fusion by KF iterations. Zhang and Xu [25] extended this method to response reconstruction under unknown input. The number and spatial arrangements of multi-type sensors were decided by adding the optimal sensor that minimized the estimation error of reconstructed responses. Li et al. [26] adopted the multi-scale attention-based neural network for sensor location selection, and the seismic response can be predicted. Nearly all the existing research regarding multi-type sensors in response reconstruction focused on optimizing sensor numbers and locations, assuming that all sensors have the same sampling frequency.

The measurement of structural displacement is a preordained but exigent task. As aforementioned, displacement could not be reliably estimated by integrating acceleration signals, and thus obtaining accurate displacement responses is genuinely challenging. Therefore, direct displacement measurement using various displacement sensors is conventionally adopted in the current SHM sensing system. Depending on the sensor installation methods, displacement can be measured in two ways. The first is the direct-contact displacement measurement using linear variable differential transducers (LVDTs), potentiometers, etc. These types of sensors measure relative displacements between two ends. Measuring absolute displacements requires a fixed platform/frame installed near the tested structures, which could be difficult, if not impractical, in real structures. Thus, contact displacement sensors are more suited to small-scale testing in a laboratory environment. The other alternative is non-contact displacement sensing, including GPS, laser displacement sensors, radar interferometry systems, and the newly developed computer-vision-based displacement tracking techniques. These sensors can record structural displacement without direct contact with the structures. Therefore, the measurement is more accessible than the contact type. One of the major problems of the non-contact displacement sensors is their low sampling rate compared with accelerometers. Most of the survey-grade GPS receivers used in SHM operate between 1 and 10 Hz [27]. With the recent advance in computer-vision techniques, displacement measurement using high-speed cameras is a propitious trend. Common ways include optical flow methods [28], template matching methods [29], and feature matching techniques [30]. Some high-speed cameras can have a frame rate of up to 1000 fps with high precision, but the price is barely affordable in civil SHM projects. The sampling frequency for standard consumer-grade cameras is usually 30 fps to 60 fps. These sampling frequencies are generally much lower than those of accelerometers. How to combine multi-type sensor data sampled at different frequencies is challenging.

Recently, some researchers have set sights on multi-rate sensor data fusion for improving displacement measurement accuracies. Smyth and Wu [31] presented a multi-rate KF approach to combine displacement and acceleration data collected simultaneously with different sampling frequencies to estimate structural displacement responses. Given that displacement signals were sampled at a lower frequency than the acceleration signals, the measurement update in KF would be conducted when displacement data were available. Otherwise, only the time update was carried out. A smoothing step was also adopted to improve accuracy. The laboratory test for data fusion of acceleration and computer-vision-based displacement sensing was completed by Chang and Xiao in 2010 [32]. This algorithm was further applied by Zhu et al. [33] in 2020 to beam-like tall buildings for data fusion of strain and acceleration data. Kim et al. [34] presented the autonomous state estimation technique considering acceleration measurement bias to enhance the computation efficiency and facilitate online monitoring. A two-stage KF was adopted, and the convergence rate of the gain matrix KF was improved compared with the previous algorithm [31]. The method was improved by defining the state vector using acceleration bias and integration error [35], and dynamic displacement can be estimated accordingly. By assuming the acceleration bias as the input vector to be estimated, Zheng et al. [36] presented an algorithm for dynamic displacement estimations based on KF. Ma et al. [37] developed an asynchronous data fusion technique to improve displacement estimation accuracies. Notably, all the abovementioned studies were designed for a single-degree-of-freedom (SDOF) system, wherein the displacement and acceleration were measured at a single point to improve displacement measurement accuracy. The response reconstruction for MDOF systems by fusing multi-type sensors sampled at different frequencies remains unexplored.

Despite recent progress in multi-type sensor data fusion, combining the multiple sampling rate data in dynamic structural response reconstruction remains to be addressed. The past investigations have several limitations: (1) Existing algorithms are designed to improve displacement measurement accuracies for an SDOF system with both accelerometer and displacement sensors installed. In practical SHM, the collocated installation of multi-type sensors is not always available. (2) Structural dynamic response reconstruction for unmonitored locations by fusing multi-rate sensor data has not been the subject of previous research. The existing techniques can be considered a model-free method to improve displacement measurement accuracy without considering structural dynamic properties. Therefore, response reconstruction through partial sensor observations is beyond the bounds of the possibility of these existing techniques.

This paper proposes a state-of-the-art multi-rate Kalman (MRKF) filtering technique for multi-type multi-rate sensor data fusion in structural dynamic response reconstruction. Data sampled at different rates, such as acceleration and displacement, are fused via two sets of observation equations. The partially observed MDOF system is allowed, and the unobserved responses will be estimated through the KF virtual sensing technique. The collocated installation requirement is relaxed in the proposed algorithm. By proposing the first structural response reconstruction algorithm with multi-rate sensor data fusion, this new method will provide a low-cost sensing solution by deploying consumer-grade cameras in real SHM projects.

The structure of this paper is organized as follows. The mathematical formulation of the algorithm is first presented, including the state-space equation, KF, MRKF, and Rauch, Tung, and Striebel (RTS) smoother. The numerical simulation of a benchmark eight-story frame is subsequently discussed. The experimental laboratory validation is presented on the basis of a cantilever beam and computer-vision-based displacement measurement using an iPhone. The response reconstruction performance and effectiveness are further examined.

2. Mathematical formulation

2.1 State-space equation

For a linear structural system with n_{DOF} DOFs, the equation of motion is frequently expressed as a second-order differential equation:

$$\mathbf{M}\ddot{\mathbf{x}}(t)+\mathbf{C}\dot{\mathbf{x}}(t)+\mathbf{K}\mathbf{x}(t)=\mathbf{S}_{\mathrm{p}}\mathbf{p}(t), \tag{1}$$

where $\ddot{\mathbf{x}}(t)\in\mathbb{R}^{n_{\mathrm{DOF}}}$, $\dot{\mathbf{x}}(t)\in\mathbb{R}^{n_{\mathrm{DOF}}}$, and $\mathbf{x}(t)\in\mathbb{R}^{n_{\mathrm{DOF}}}$ are the nodal acceleration, velocity, and displacement vectors, respectively. Structural dynamic responses depend on external loads , mass matrix $\mathbf{M}\in\mathbb{R}^{n_{\mathrm{DOF}}\times n_{\mathrm{DOF}}}$, damping matrix $\mathbf{C}\in\mathbb{R}^{n_{\mathrm{DOF}}\times n_{\mathrm{DOF}}}$, and stiffness matrix $\mathbf{K}\in\mathbb{R}^{n_{\mathrm{DOF}}\times n_{\mathrm{DOF}}}$. These matrices are commonly used in structural dynamics to mathematically model the behavior of dynamic systems. By formulating and solving equations involving these matrices, it becomes possible to predict and analyze the response of the system to various excitations. $\mathbf{S}_{\mathrm{p}}\in\mathbb{R}^{n_{\mathrm{DOF}}\times n_{\mathrm{p}}}$ is the spatial distribution matrix for the external load $\mathbf{p}(t)$, and its nonzero entries relate to the DOFs corresponding to the load.

By augmenting structural nodal displacement and velocity, the state vector can be written as $\mathbf{z}(t)=\begin{Bmatrix}\mathbf{x}(t)\\ \dot{\mathbf{x}}(t)\end{Bmatrix}$. The equation (1) can therefore be rewritten in a first-order differential form:

$$\dot{\mathbf{z}}(t)=\mathbf{A}_{\mathrm{c}}\mathbf{z}(t)+\mathbf{B}_{\mathrm{c}}\mathbf{p}(t), \tag{2}$$

$$\mathbf{y}(t)=\mathbf{C}_{\mathrm{c}}\mathbf{z}(t)+\mathbf{D}_{\mathrm{c}}\mathbf{p}(t). \tag{3}$$

Equation (2) is the state equation, in which $\mathbf{A}_{\mathrm{c}}\in\mathbb{R}^{2n_{\mathrm{DOF}}\times 2n_{\mathrm{DOF}}}$ is the system matrix, and $\mathbf{B}_{\mathrm{c}}\in\mathbb{R}^{2n_{\mathrm{DOF}}\times n_{\mathrm{p}}}$ is the input matrix. The subscript *c* stands for continuous time. The observation equation (3) is expressed by the output influence matrix $\mathbf{C}_{\mathrm{c}}\in\mathbb{R}^{n_{\mathrm{y}}\times 2n_{\mathrm{DOF}}}$, and the input feedthrough matrix . $\mathbf{D}_{\mathrm{c}}\in\mathbb{R}^{n_{\mathrm{y}}\times n_{\mathrm{p}}}$.. Without loss of generality, we can consider that the observation vector $\mathbf{y}(t)\in\mathbb{R}^{n_{\mathrm{y}}}$ includes structural displacement, velocity, and acceleration, which can be obtained on the basis of the spatial selection matrices $\mathbf{S}_{\mathrm{dis}}\in\mathbb{R}^{n_{\mathrm{dis}}\times n_{\mathrm{DOF}}}$, $\mathbf{S}_{\mathrm{v}}\in\mathbb{R}^{n_{\mathrm{vel}}\times n_{\mathrm{DOF}}}$, and $\mathbf{S}_{\mathrm{a}}\in\mathbb{R}^{n_{\mathrm{acc}}\times n_{\mathrm{DOF}}}$, respectively. These matrices can be regarded as Boolean matrices represented by 0s and 1s, where 0 represents false (no sensor at this DOF) and 1 represents true (has a sensor at this DOF). The dimensions of these selection matrices are determined by the sensor number and structural DOFs.

$$\mathbf{y}(t)=\begin{bmatrix}\mathbf{S}_{\mathrm{dis}} & \mathbf{0} & \mathbf{0}\\ \mathbf{0} & \mathbf{S}_{\mathrm{v}} & \mathbf{0}\\ \mathbf{0} & \mathbf{0} & \mathbf{S}_{\mathrm{a}}\end{bmatrix}\begin{bmatrix}\mathbf{x}(t)\\ \dot{\mathbf{x}}(t)\\ \ddot{\mathbf{x}}(t)\end{bmatrix}, \tag{4}$$

Therefore, the state-space matrices can be written as

$$\mathbf{A}_{\mathrm{c}}=\begin{bmatrix}\mathbf{0}_{n_{\mathrm{DOF}}} & \mathbf{I}_{n_{\mathrm{DOF}}}\\ -\mathbf{M}^{-1}\mathbf{K} & -\mathbf{M}^{-1}\mathbf{C}\end{bmatrix},\quad \mathbf{B}_{\mathrm{c}}=\begin{bmatrix}\mathbf{0}_{n_{\mathrm{DOF}}}\\ \mathbf{M}^{-1}\mathbf{S}_{\mathrm{p}}\end{bmatrix}, \tag{5}$$

$$\mathbf{C}_{\mathrm{c}}=\begin{bmatrix}\mathbf{S}_{\mathrm{dis}} & \mathbf{0}\\ \mathbf{0} & \mathbf{S}_{\mathrm{v}}\\ -\mathbf{S}_{\mathrm{a}}\mathbf{M}^{-1}\mathbf{K} & -\mathbf{S}_{\mathrm{a}}\mathbf{M}^{-1}\mathbf{C}\end{bmatrix},\quad \mathbf{D}_{\mathrm{c}}=\begin{bmatrix}\mathbf{0}\\ \mathbf{0}\\ \mathbf{S}_{\mathrm{a}}\mathbf{M}^{-1}\mathbf{S}_{\mathrm{p}}\end{bmatrix}, \tag{6}$$

where the input feedthrough matrix $\mathbf{D}_{\mathrm{c}}$ in the observation equation is nonzero only if accelerations are measured.

In SHM applications, structure responses are digitalized by a data acquisition system with prespecified sampling frequencies. The continuous state-space model in equations (2) and (3) should be transferred into discrete difference equations to facilitate numerical calculation. Given a sampling interval Δt, the discrete state-space model reads as follows:

$$\mathbf{z}_{k+1} = \mathbf{A}_k \mathbf{z}_k + \mathbf{B}_k \mathbf{p}_k + \mathbf{w}_k , \tag{7}$$

$$\mathbf{y}_k = \mathbf{C}_k \mathbf{z}_k + \mathbf{D}_k \mathbf{p}_k + \boldsymbol{\upsilon}_k . \tag{8}$$

The discrete system matrix $\mathbf{A}_k$ and input matrix $\mathbf{B}_k$ are calculated by the following:

$$\mathbf{A}_k = \mathbf{e}^{\mathbf{A}_{\mathrm{c}} \Delta t} , \tag{9}$$

$$\mathbf{B}_k = \left[\mathbf{A}_k - \mathbf{I} \right] \mathbf{A}_{\mathrm{c}}{}^{-1} \mathbf{B}_{\mathrm{c}} . \tag{10}$$

Assuming zero-order-hold (ZOH) for external input $\mathbf{p}_k$, the discrete output influence matrix $\mathbf{C}_k = \mathbf{C}_{\mathrm{c}}$, and the discrete input feedthrough matrix $\mathbf{D}_k = \mathbf{D}_{\mathrm{c}}$. System error $\mathbf{w}_k$ and measurement noises $\boldsymbol{\upsilon}_k$ are assumed as independent normally distributed white noises. The noise matrices are defined by the system error covariance matrix $\mathrm{E}\left[\mathbf{w}_k \mathbf{w}_k^{\mathrm{T}} \right] = \mathbf{Q}$ and measurement noise error covariance matrix $\mathrm{E}\left[\boldsymbol{\upsilon}_k \boldsymbol{\upsilon}_k^{\mathrm{T}} \right] = \mathbf{R}$.

2.2 Kalman filtering

KF is an unbiased estimator based on the least-square technique considering system and measurement uncertainties. The KF calculation includes two steps: the time update and the measurement update of the state vector. Through these two-step recursive iterations, the minimum-variance-unbiased state estimation $\hat{\mathbf{z}}_{k/k}$ could be obtained.

Time update of state vector

$$\hat{\mathbf{z}}_{k/k-1} = \mathbf{A}_{k-1} \hat{\mathbf{z}}_{k-1/k-1} + \mathbf{B}_{k-1} \mathbf{p}_{k-1} , \tag{11}$$

$$\mathbf{P}_{k/k-1} = \mathbf{A}_{k-1} \mathbf{P}_{k-1/k-1} \mathbf{A}_{k-1}^{\mathrm{T}} + \mathbf{Q}_{k-1} . \tag{12}$$

Measurement update of state vector

$$\mathbf{K}_k = \mathbf{P}_{k/k-1} \mathbf{C}_k^{\mathrm{T}} \left(\mathbf{C}_k \mathbf{P}_{k/k-1} \mathbf{C}_k^{\mathrm{T}} + \mathbf{R}_k \right)^{-1} , \tag{13}$$

$$\hat{\mathbf{z}}_{k/k} = \hat{\mathbf{z}}_{k/k-1} + \mathbf{K}_k \left(\mathbf{y}_k - \mathbf{C}_k \hat{\mathbf{z}}_{k/k-1} - \mathbf{D}_k \mathbf{p}_k \right) , \tag{14}$$

$$\mathbf{P}_{k/k} = \left(\mathbf{I} - \mathbf{K}_k \mathbf{C}_k \right) \mathbf{P}_{k/k-1} \left(\mathbf{I} - \mathbf{K}_k \mathbf{C}_k \right)^{\mathrm{T}} + \mathbf{K}_k \mathbf{R}_k \mathbf{K}_k^{\mathrm{T}} , \tag{15}$$

where $\mathbf{P}_{k|k} = \mathrm{E}\left[\left(\mathbf{z}_k - \hat{\mathbf{z}}_{k|k}\right)\left(\mathbf{z}_k - \hat{\mathbf{z}}_{k|k}\right)^{\mathrm{T}}\right]$ refers to the covariance matrix of the state estimation error, and $\mathbf{K}_k$ is the Kalman gain matrix.

2.3 MRKF with RTS smoother

Considering a representative case in SHM, the observation vector includes displacement and acceleration measurements, and their sampling frequencies are *SF_acc* and *SF_dis*, respectively. Usually, the sampling frequency of the accelerometers is several times that of the displacement sensors. Therefore, we define *N = SF_acc / SF_dis.* That is, at a certain time point *k*, only acceleration measurement $\mathbf{y}_{\mathrm{acc}} \in \mathbb{R}^{n_{\mathrm{a}}}$ is available. Based on the availability of displacement measurement, two sets of observation vectors are defined as follows:

$$\mathbf{y}_{\mathrm{acc}} = \mathbf{S}_{\mathrm{a}}\ddot{\mathbf{x}}(t), \tag{16}$$

$$\mathbf{y}_{\mathrm{com}} = \begin{bmatrix} \mathbf{S}_{\mathrm{dis}} & \mathbf{0} \\ \mathbf{0} & \mathbf{S}_{\mathrm{a}} \end{bmatrix} \begin{bmatrix} \mathbf{x}(t) \\ \ddot{\mathbf{x}}(t) \end{bmatrix}, \tag{17}$$

where $\mathbf{y}_{\mathrm{com}} \in \mathbb{R}^{n_{\mathrm{dis}}+n_{\mathrm{a}}}$ includes both displacement and acceleration measurements, and $\mathbf{S}_{\mathrm{dis}}$ and $\mathbf{S}_{\mathrm{a}}$ are the selection matrices for displacement and acceleration measurements, respectively.

The observation equation in equation (8) can be rewritten as follows:

$$\mathbf{y}_{\mathrm{acc},k} = \mathbf{C}_{\mathrm{acc},k}\mathbf{z}_k + \mathbf{D}_{\mathrm{acc},k}\mathbf{p}_k + \boldsymbol{\upsilon}_{\mathrm{acc},k}, \tag{18}$$

$$\mathbf{y}_{\mathrm{com},k} = \mathbf{C}_{\mathrm{com},k}\mathbf{z}_k + \mathbf{D}_{\mathrm{com},k}\mathbf{p}_k + \boldsymbol{\upsilon}_{\mathrm{com},k}, \tag{19}$$

where $\mathbf{C}_{\mathrm{acc},k} = \begin{bmatrix} -\mathbf{S}_{\mathrm{a}}\mathbf{M}^{-1}\mathbf{K} & -\mathbf{S}_{\mathrm{a}}\mathbf{M}^{-1}\mathbf{C} \end{bmatrix}$, $\mathbf{D}_{\mathrm{acc},k} = \mathbf{S}_{\mathrm{a}}\mathbf{M}^{-1}\mathbf{S}_{\mathrm{p}}$, $\mathbf{C}_{\mathrm{com},k} = \begin{bmatrix} \mathbf{S}_{\mathrm{dis}} & \mathbf{0} \\ -\mathbf{S}_{\mathrm{a}}\mathbf{M}^{-1}\mathbf{K} & -\mathbf{S}_{\mathrm{a}}\mathbf{M}^{-1}\mathbf{C} \end{bmatrix}$, and $\mathbf{D}_{\mathrm{com},k} = \begin{bmatrix} \mathbf{0} \\ \mathbf{S}_{\mathrm{a}}\mathbf{M}^{-1}\mathbf{S}_{\mathrm{p}} \end{bmatrix}$.

The time update of state vector equations (11)–(12) will be conducted for each time step *k*. If only acceleration observation is available, the measurement update of the state vector will be conducted on the basis of equation (18). Otherwise, equation (19) will be adopted.

The smoothing process is generally used in offline calculations, where future measurements beyond the current time point are used to generate better state estimation. The RTS smoother was proposed by Rauch, Tung, and Striebel in 1965 [38] and is a commonly used fixed-interval smoother. The interval for RTS smoothing c_{RTS} shall be pre-defined. When c_{RTS} is small, the RTS smoother is nearly online. However, c_{RTS} shall be long enough for the smoother to obtain stable results. Thus, c_{RTS} should be determined in consideration of computational accuracy and time delay. Given the state estimation up to time *tt*, for $k = tt\text{-}c_{\mathrm{RTS}}$ to *tt*-1, the smoothing process is accomplished by first initializing the state vector $\hat{\mathbf{z}}_{\mathrm{b},tt} = \hat{\mathbf{z}}_{\mathrm{b},k+1} = \hat{\mathbf{z}}_{\mathrm{f},k+1/k+1}$ and covariance matrix $\mathbf{P}_{\mathrm{b},tt} = \mathbf{P}_{\mathrm{b},k+1} = \mathbf{P}_{\mathrm{f},k+1}$, where the subscript *f* refers to the forward KF calculated using equations (11)–(19). The optimized state estimation after the RTS smoothing $\hat{\mathbf{z}}_{\mathrm{b},k}$ can be obtained by conducting another backward KF iteration from $k = tt\text{-}1$ to $k = tt\text{-}c_{\mathrm{RTS}}$. The calculation steps for RTS smoothing are presented in equations (20)–(23).

$$\mathbf{I}_{\mathrm{b},k+1/k} = \left(\mathbf{P}_{\mathrm{f},k+1/k}\right)^{-1}, \tag{20}$$

$$\mathbf{K}_{\mathrm{b},k} = \mathbf{P}_{\mathrm{f},k/k}\mathbf{A}_k^{\mathrm{T}}\mathbf{I}_{\mathrm{b},k+1/k}, \tag{21}$$

$$\mathbf{P}_{\mathrm{b},k} = \mathbf{P}_{\mathrm{f},k/k} - \mathbf{K}_{\mathrm{b},k}\left(\mathbf{P}_{\mathrm{f},k+1/k} - \mathbf{P}_{\mathrm{b},k+1}\right)\mathbf{K}_{\mathrm{b},k}^{\mathrm{T}}, \tag{22}$$

$$\hat{\mathbf{z}}_{\mathrm{b},k} = \hat{\mathbf{z}}_{\mathrm{f},k/k} + \mathbf{K}_{\mathrm{b},k}\left(\hat{\mathbf{z}}_{\mathrm{b},k+1} - \hat{\mathbf{z}}_{\mathrm{f},k+1/k}\right). \tag{23}$$

Table 1 summarizes the detailed iteration steps.

Table 1

MRKF with RTS smoothing

Calculation steps
1. Initialization at time t_0:
2. MRKF Iteration with RTS smoothing
for *i* = 1: SF_dis×t (total displacement measurements)
m = (*i*-1) × *N*
for *k* = 1: *N*
● time update of state vector

```
        $\hat{\mathbf{z}}_{\mathrm{f},m+k/m+k-1} = \mathbf{A}_{m+k-1}\hat{\mathbf{z}}_{\mathrm{f},m+k-1/m+k-1} + \mathbf{B}_{m+k-1}\mathbf{p}_{m+k-1}$
        $\mathbf{P}_{\mathrm{f},m+k/m+k-1} = \mathbf{A}_{m+k-1}\mathbf{P}_{\mathrm{f},m+k-1/m+k-1}\mathbf{A}^{\mathrm{T}}_{m+k-1} + \mathbf{Q}_{m+k-1}$
        if (k < N)
        ■   measurement update by acceleration observation
            $\mathbf{K}_{\mathrm{f},m+k} = \mathbf{P}_{\mathrm{f},m+k/m+k-1}\mathbf{C}^{\mathrm{T}}_{\mathrm{acc},m+k}\left(\mathbf{C}_{\mathrm{acc},m+k}\mathbf{P}_{\mathrm{f},m+k/m+k-1}\mathbf{C}^{\mathrm{T}}_{\mathrm{acc},m+k} + \mathbf{R}_{\mathrm{acc},m+k}\right)^{-1}$
            $\hat{\mathbf{z}}_{\mathrm{f},m+k/m+k} = \hat{\mathbf{z}}_{\mathrm{f},m+k/m+k-1} + \mathbf{K}_{\mathrm{f},m+k}\left(\mathbf{y}_{\mathrm{acc},m+k} - \mathbf{C}_{\mathrm{acc},m+k}\hat{\mathbf{z}}_{\mathrm{f},m+k/m+k-1} - \mathbf{D}_{\mathrm{acc},m+k}\mathbf{p}_{m+k}\right)$
            $\mathbf{P}_{\mathrm{f},m+k/m+k} = \left(\mathbf{I} - \mathbf{K}_{\mathrm{f},m+k}\mathbf{C}_{\mathrm{acc},m+k}\right)\mathbf{P}_{\mathrm{f},m+k/m+k-1}\left(\mathbf{I} - \mathbf{K}_{\mathrm{f},m+k}\mathbf{C}_{\mathrm{acc},m+k}\right)^{\mathrm{T}} + \mathbf{K}_{\mathrm{f},m+k}\mathbf{R}_{\mathrm{acc},m+k}\mathbf{K}^{\mathrm{T}}_{\mathrm{f},m+k}$

        else (k = N)
        ■   measurement update by displacement and acceleration observation
            $\mathbf{K}_{\mathrm{f},m+k} = \mathbf{P}_{\mathrm{f},m+k/m+k-1}\mathbf{C}^{\mathrm{T}}_{\mathrm{com},m+k}\left(\mathbf{C}_{\mathrm{com},m+k}\mathbf{P}_{\mathrm{f},m+k/m+k-1}\mathbf{C}^{\mathrm{T}}_{\mathrm{com},m+k} + \mathbf{R}_{\mathrm{com},m+k}\right)^{-1}$
            $\hat{\mathbf{z}}_{\mathrm{f},m+k/m+k} = \hat{\mathbf{z}}_{\mathrm{f},m+k/m+k-1} + \mathbf{K}_{\mathrm{f},m+k}\left(\mathbf{y}_{\mathrm{com},m+k} - \mathbf{C}_{\mathrm{com},m+k}\hat{\mathbf{z}}_{\mathrm{f},m+k/m+k-1} - \mathbf{D}_{\mathrm{com},m+k}\mathbf{p}_{m+k}\right)$
            $\mathbf{P}_{\mathrm{f},m+k/m+k} = \left(\mathbf{I} - \mathbf{K}_{\mathrm{f},m+k}\mathbf{C}_{\mathrm{com},m+k}\right)\mathbf{P}_{\mathrm{f},m+k/m+k-1}\left(\mathbf{I} - \mathbf{K}_{\mathrm{f},m+k}\mathbf{C}_{\mathrm{com},m+k}\right)^{\mathrm{T}} + \mathbf{K}_{\mathrm{f},m+k}\mathbf{R}_{\mathrm{com},m+k}\mathbf{K}^{\mathrm{T}}_{\mathrm{f},m}$

         end
    end

    ●   RTS smoothing at pre-defined interval $c_{\mathrm{RTS}}$

    if remainder($i$, $c_{\mathrm{RTS}}$) = 0

        $\hat{\mathbf{z}}_{\mathrm{b},i\times N} = \hat{\mathbf{z}}_{\mathrm{f},i\times N/i\times N}$
        $\mathbf{P}_{\mathrm{b},i\times N} = \mathbf{P}_{\mathrm{f},i\times N/i\times N}$

        for $j$ = 1: $c_{\mathrm{RTS}} \times N$ - 1

            $\mathbf{I}_{\mathrm{b},i\times N-j+1/i\times N-j} = \left(\mathbf{P}_{\mathrm{f},i\times N-j+1/i\times N-j}\right)^{-1}$
            $\mathbf{K}_{\mathrm{b},i\times N-j} = \mathbf{P}_{\mathrm{f},i\times N-j/i\times N-j}\mathbf{A}^{\mathrm{T}}_{i\times N-j}\mathbf{I}_{b,i\times N-j+1/i\times N-j}$
            $\mathbf{P}_{\mathrm{b},i\times N-j} = \mathbf{P}_{\mathrm{f},i\times N-j/i\times N-j} - \mathbf{K}_{\mathrm{b},i\times N-j}\left(\mathbf{P}_{\mathrm{f},i\times N-j+1/i\times N-j} - \mathbf{P}_{\mathrm{b},i\times N-j+1}\right)\mathbf{K}^{\mathrm{T}}_{\mathrm{b},i\times N-j}$
            $\hat{\mathbf{z}}_{\mathrm{b},i\times N-j} = \hat{\mathbf{z}}_{\mathrm{f},i\times N-j/i\times N-j} + \mathbf{K}_{\mathrm{b},i\times N-j}\left(\hat{\mathbf{z}}_{\mathrm{b},i\times N-j+1} - \hat{\mathbf{z}}_{\mathrm{f},i\times N-j+1/i\times N-j}\right)$

        end
    end
end
```

3. Numerical examples

3.1. Eight-story shear frame model

This section adopts the eight-story shear frame presented by Callafon et al. [39] and Azam et al. [40] to verify the capability and robustness of the proposed algorithm. As shown in Fig. 1, the 2-D frame has a uniform floor mass of 625,000 kg. The lateral story stiffness provided by two columns is 10^6 kN/m. The damping ratio is 2% for all modes. Table 2 presents the undamped natural frequencies of this frame.

Table 2

Undamped natural frequencies of the eight-story frame

Mode No.	1	2	3	4	5	6	7	8
Frequency (Hz)	1.17	3.48	5.67	7.67	9.41	10.83	11.87	12.52

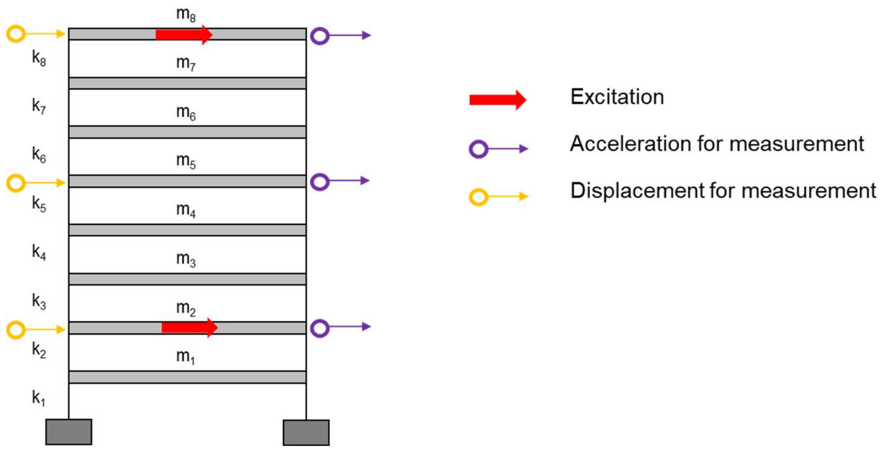

Fig. 1. Overview of the eight-story 2D shear frame

3.2 Baseline analysis

As aforementioned, accelerometers in SHM usually operate at high frequencies to capture the structure's high-order modes, and thus the sampling frequencies shall be determined according to the tested structure's natural frequencies; whereas displacements are commonly measured at relatively lower sampling frequencies (1-10 Hz for traditional GPS and 30-60 Hz for consumer-grade cameras). Therefore, in the baseline numerical case, data fusion for 100 Hz acceleration and 5 Hz displacement measurement is conducted. Three displacement sensors and three accelerometers are installed along the frame height, as shown in Fig. 1.

Table 3 presents six different fusion schemes adopted to verify the filter performance. Schemes 1 and 2 are designed to reconstruct structural responses by only one sensor type. Schemes 3 and 4 are traditional data fusion techniques based on a single sampling frequency, wherein Scheme 3 uses the low sampling frequency of the displacement measurements. Scheme 5 presents the proposed MRKF algorithm without the RTS smoother, whereas Scheme 6 presents the performance of the MRKF with the RTS smoother. Notably, Schemes 1 to 4 are not designed for multi-rate data fusion; thus, the traditional KF can be applied. MRKF algorithm have to be adopted in Schemes 5 and 6.

Table 3

Detailed information of comparison schemes

Scheme		Sampling frequency (Hz)	
		Acceleration	Displacement
1	Acceleration only	100	N/A
2	Displacement only	N/A	5
3	Single rate (low)	5	5
4	Single rate (high)	100	100
5	MRKF	100	5
6	MRKF+RTS	100	5

In this baseline case, the excitation applied on DOF2 has a frequency range of 0.01–20 Hz, whereas that on DOF8 has 20–50 Hz. The amplitude is 2000 kN for both excitations. The excitation frequency range is designed to cover the natural frequencies of the shear frame. Collocated monitoring is adopted in this baseline numerical case. Accelerations and displacements are monitored on DOF2, DOF5, and DOF8. In this simulation, the measurement noise and system noise are calculated in consideration of the variance of the structural responses. Random measurement noise, whose standard deviation σ is calculated as 5% of the response standard deviation, is added to the theoretical responses to obtain noise-corrupted observations. The measurement noise covariance matrix $\mathbf{R}_k$ is obtained on the basis of σ^2. Similarly, the system noise covariance matrix $\mathbf{Q}_k$ is also calculated on the basis of 5% of the standard deviation of state vectors. The RTS interval c_{RTS} is assumed as 5 in this baseline analysis, which means RTS smoothing is conducted for every 5 displacement observations.

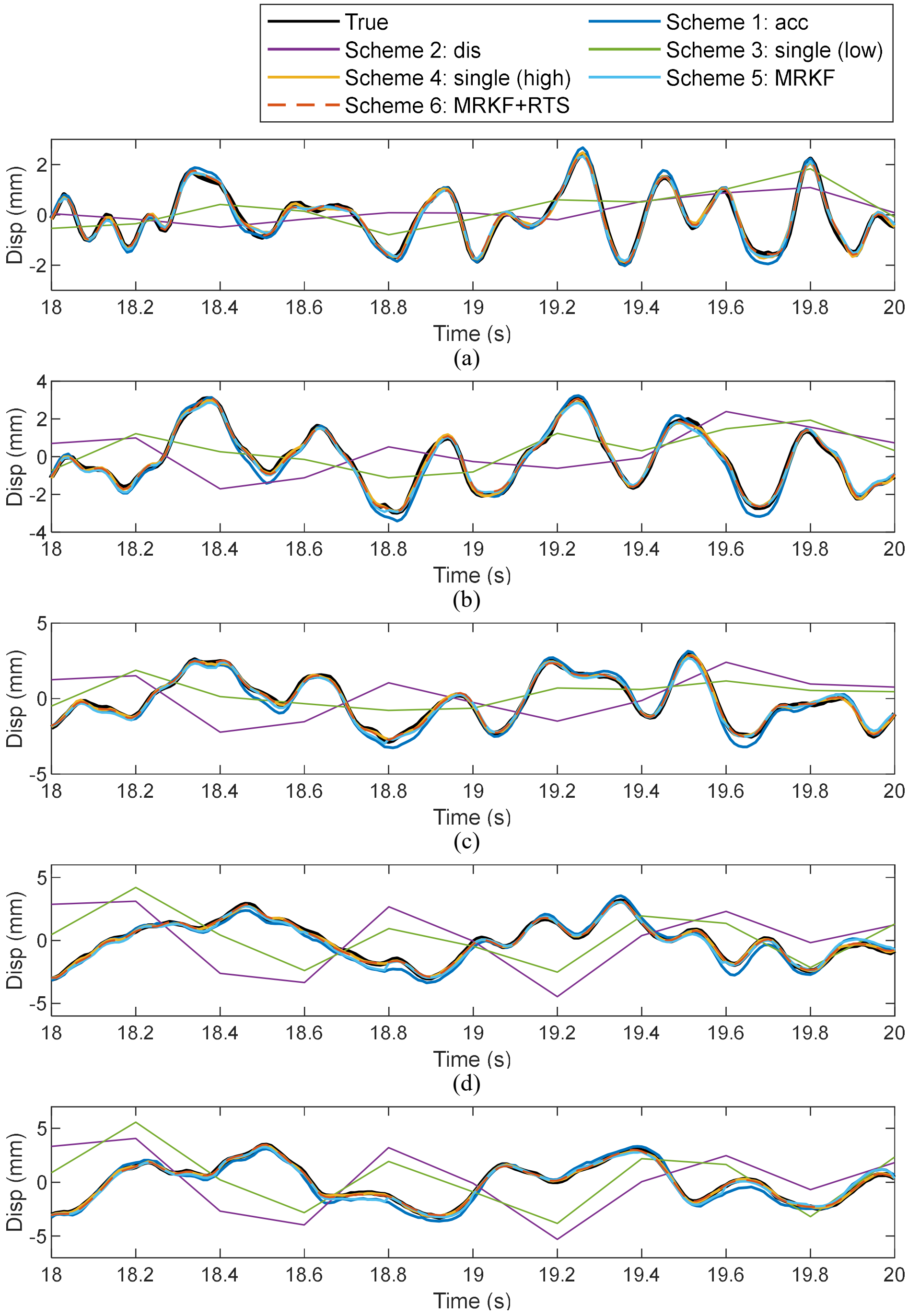

(a)

(b)

(c)

(d)

(e)

Fig. 2. Displacement reconstruction results at verification DOFs in numerical baseline case (a) DOF1, (b) DOF3, (c) DOF4, (d) DOF6, and (e) DOF7

Fig. 2 compares the time histories of the reconstructed displacement responses using different schemes. At DOF1, DOF3, DOF4, DOF6, and DOF7, neither displacement nor acceleration is monitored, and the responses are estimated from response reconstruction. Scheme 2 (i.e., response reconstruction by displacement only) fails to produce reasonable results. This failure happens because the discretization of the system matrix $\mathbf{A}_k$ and the input matrix $\mathbf{B}_k$ are based on the sampling interval Δt, as presented in equations (9) and (10). Low sampling frequency leads to inaccuracies in the discretization process (e.g., in $\mathbf{A}_k$ and $\mathbf{B}_k$ matrices) and losses the ability to track high-frequency structural responses. The same explanation holds for the results of response reconstruction in Scheme 3 using a single low sampling rate. Scheme 1 uses acceleration observations only, and thus the displacement estimation obtained has relatively large errors. The remaining three schemes (Schemes 4-6) have competitive performances. Scheme 4 has the best performance among different schemes because of its high sampling rates in both acceleration and displacement measurements. Since Scheme 5 uses much less available displacement measurements in MRKF than Scheme 4, the former exhibits larger estimation errors than the latter. However, after the RTS smoothing procedure, the reconstruction errors are reduced effectively in Scheme 6 because more future observations are used in the current estimations. Fig. 3 illustrates the reconstructed time histories of the acceleration and velocity responses at DOF7 using different schemes, wherein only 2-s duration is presented to illustrate the comparison clearly. Fig. 4 shows the corresponding reconstruction errors compared with the real value. The proposed MRKF algorithm with RTS smoothing (i.e., Scheme 6) can achieve satisfactory response reconstruction results and substantially reduce the errors, compared with the results based on one sensor type (i.e., Schemes 1 and 2) and single low sampling frequency data fusion (Scheme 3). The MRKF algorithm alone (Scheme 5) can estimate acceleration responses accurately; however, its reconstructed displacements exhibit apparently larger errors than Scheme 4, because of the low sampling rate in displacement observations in Scheme 5. After

RTS smoothing, the response reconstruction accuracy has been considerably improved in Scheme 6, especially for the displacement reconstruction. The performance of MRKF+RTS (Scheme 6) is nearly the same as the traditional data fusion with high sampling frequencies for both acceleration and displacement (i.e., Scheme 4).

Fig. 5 presents the acceleration reconstruction results in the frequency domain at DOF7. Except Scheme 2 (i.e., displacement only) and Scheme 3 (i.e., single rate low), all other schemes can successfully capture the first two natural frequencies of the frame. However, more oscillations are observed in the reconstructed spectra by Scheme 1 (i.e., acceleration only) and Scheme 5 (MRKF algorithm), especially in the range of 0 to 10 Hz. After RTS smoothing, the proposed Scheme 6 show comparable performance with Scheme 4, both of which agree well with the true value. The multi-rate sensor data fusion technique in structural response reconstruction deserves further research efforts.

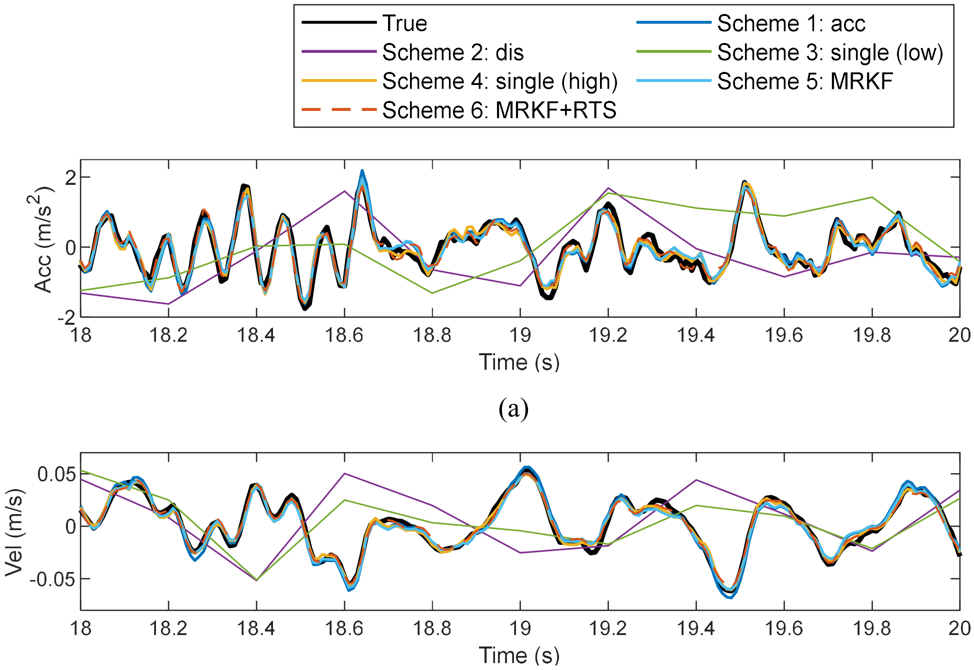

(a)

(b)

Fig. 3. Response reconstruction results at DOF7 in numerical baseline case: (a) acceleration and (b) velocity

Normalized root mean square error (NRMSE) is adopted as the performance indicator in the quantitative comparison of the filter performance. Root mean square error (RMSE) is first calculated to assess the accuracy of state estimation $\hat{x}_k$ compared with real response x_k .

$$RMSE = \sqrt{\frac{\sum_{k=1}^{n}\left(x_k - \hat{x}_k\right)^2}{n}}, \tag{24}$$

NRMSE is further defined to facilitate comparing different DOFs and scenarios. The RMSE is normalized by the difference between maximum and minimum values to obtain NRMSE in this paper. A smaller NRMSE indicates higher precision.

$$NRMSE = \frac{RMSE}{x_{\max} - x_{\min}}. \tag{25}$$

Table 4 shows the steady-state NRMSE for displacement obtained by different schemes (as described in Table 3) in this baseline analysis. Response reconstruction by displacement only (Scheme 2) has the worst performance because of the discretization problem. The failure of response reconstruction by a single rate (low) (Scheme 3) proves that the down-sampling-based data fusion technique is problematic, though it is a common practice when signals are sampled at different frequencies. It is unsurprising that the single rate (high) (Scheme 4) generally has the best accuracy because both accelerations and displacements are sampled at 100 Hz. In comparison, the proposed MRKF algorithm with RTS (Scheme 6) has extremely competitive performances for most of the DOFs, which implies that a high sampling frequency of displacement observation is unnecessary given the proposed MRKF. Notably, the responses at DOF2, DOF5, and DOF8, are directly measured by displacement sensors and accelerometers. The NRMSEs for the displacements at these three DOFs are 1.323%, 1.168%, and 0.841%, respectively, which are even lower than measurement noise. Thus, the estimated displacements at three DOFs are more accurate than the direct measurements by sensors.

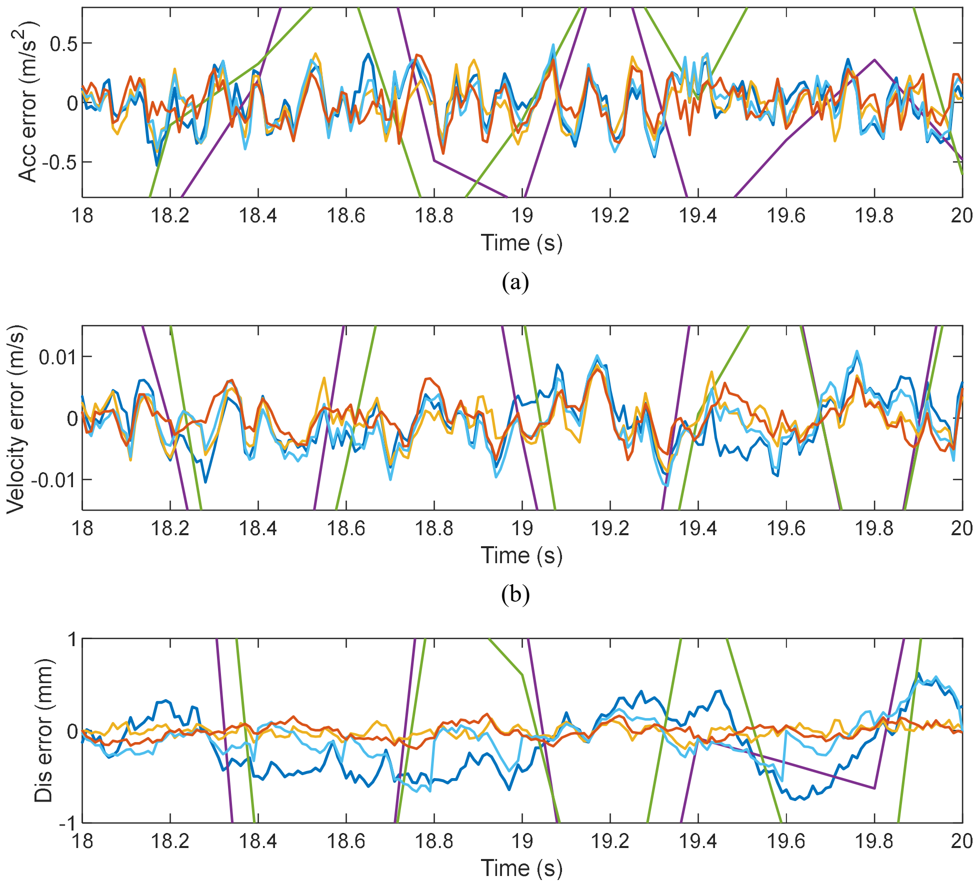

(a)

(b)

(c)

Fig. 4. Comparison of reconstruction errors at DOF7 in numerical baseline case: (a) acceleration, (b) velocity, and (c) displacement

The comparison between Scheme 1 and Scheme 5 indicates that given the MRKF algorithm, even adding low-sampling-rate displacement measurements to acceleration measurements can considerably improve the estimation accuracy by 13% to 43%. The comparison between Scheme 5 and Scheme 6 indicates that the RTS smoothing process can further reduce the estimation error by approximately 20% to 50%. The NRMSE for velocity is similar to the displacement results and therefore omitted for the sake of brevity.

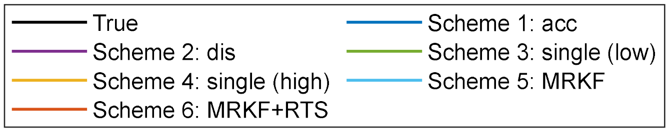

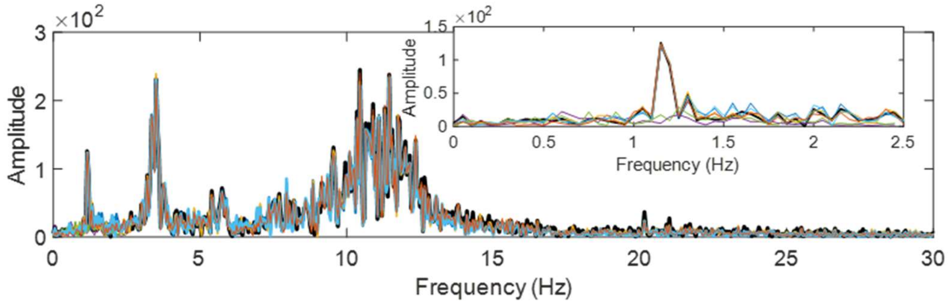

Fig. 5. Comparison of the reconstructed acceleration results in the frequency domain at DOF7 in numerical baseline case: (a) 0–30 Hz and (b) 0–2.5 Hz

Table 4

Steady-state NRMSE for displacement obtained by different schemes in the numerical baseline case

Scheme		NRMSE for displacement (%)							
		DOF1	DOF2[a]	DOF3	DOF4	DOF5[a]	DOF6	DOF7	DOF8[a]
1	Acc only	2.863	2.190	2.843	3.303	3.468	3.639	3.499	3.135
2	Dis only	22.60	23.94	28.13	31.39	30.37	33.30	32.67	29.01
3	Single rate (low)	18.77	17.70	22.37	23.36	23.17	24.92	24.76	21.62
4	Single rate (high)	2.012	0.761	1.199	1.092	0.605	0.914	0.586	0.492
5	MRKF	2.500	1.530	1.987	2.081	1.979	2.143	2.044	1.837
6	MRKF+RTS	1.837	0.933	1.258	1.211	0.900	1.039	0.974	0.868

[a]: These DOFs are directly measured by sensors.

Table 5 presents the acceleration estimation results. The NRMSEs at the three DOFs with accelerometers are 0.612%, 0.993%, and 0.702% in Scheme 1, which are slightly smaller than sensor measurement noise. The good performance of Scheme 1 indicates that reconstructing acceleration by using accelerometer measurements only can produce reasonable results. MRKF has a comparable performance with Scheme 1. However, the reconstruction errors can be considerably reduced after the RTS smoothing. The estimation errors in Scheme 6 are even smaller than those obtained through high-frequency data fusion (Scheme 4). Acceleration reconstructions in Schemes 2 and 3 are unsatisfactory because capturing high-order structural vibrations through low-frequency observations is difficult.

Fig. 6 plots the data presented in Tables 4 and 5 to provide a clear comparison of estimation accuracies. The proposed algorithm with RTS smoothing achieves superior reconstruction accuracy even without high-frequency displacement measurements. The comparison confirms that, given the proposed MRKF+RTS algorithm, a high sampling frequency of displacement observation is unnecessary.

Table 5

Steady-state NRMSE for acceleration obtained by different schemes in the numerical baseline case

Sensing scheme		NRMSE for acceleration (%)							
		DOF1	DOF2[a]	DOF3	DOF4	DOF5[a]	DOF6	DOF7	DOF8[a]
1	Acc only	3.231	0.612	4.092	4.524	0.993	4.194	3.577	0.702
2	Dis only	15.42	16.31	19.34	21.02	22.87	18.46	21.91	14.73
3	Single rate (low)	12.42	2.401	14.50	15.20	3.191	14.00	18.62	3.626
4	Single rate (high)	3.036	0.603	3.814	4.219	0.979	4.034	3.057	0.681
5	MRKF	3.237	1.707	4.163	4.538	1.271	4.197	3.566	1.441
6	MRKF+RTS	2.557	0.561	3.320	3.707	0.934	3.241	2.668	0.622

[a]: These DOFs are directly measured by sensors.

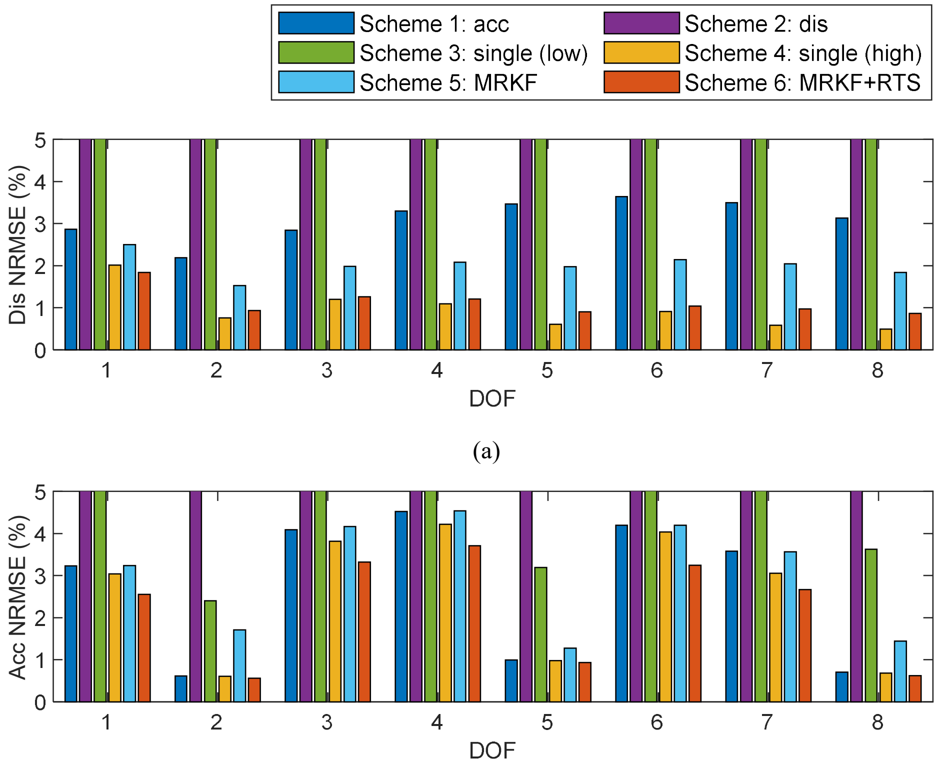

(a)

(b)

Fig.6. NRMSE in the numerical baseline case: (a) displacement, (b) acceleration

3.3 Parametric analysis

Seven cases (Cases 2–8) are designed and compared with the baseline analysis (Case 1) to examine the filter robustness and performance under different scenarios. Different influencing factors are considered in the simulations. Considering that the displacement sampling frequency varies with different sensor types, Case 2 is designed to check filter performance with displacement observations sampled at a relatively higher frequency (i.e., 50 Hz). In Case 3, two random loadings are replaced by a harmonic excitation of 10 Hz plus a combination of harmonic excitations of 0.1 Hz and 50 Hz. The comparison between Cases 1 and 4 aims to examine the influence of the number of excitations. Case 5 considers the non-collocated sensor arrangement (i.e., the accelerometer and displacement sensor are installed at different DOFs). The different levels of measurement noise (Case 1 vs. Case 6) and system noise (Case 1 vs. Case 7) are studied. In Case 8, c_{RTS} is set to 1, which means RTS smoothing is conducted for every displacement measurement.

Table 6. Simulation cases in verification analysis

Case	Input location	Input type	Sampling frequency (Hz)		c_{RTS}	Sensor location		Measurement noise	System noise
			acc	dis		acc	dis		
1	2 8	random	100	5	5	2 5 8	2 5 8	5%	5%
2	2 8	random	100	50	5	2 5 8	2 5 8	5%	5%
3	2 8	harmonic	100	5	5	2 5 8	2 5 8	5%	5%
4	2 5 8	random	100	5	5	2 5 8	2 5 8	5%	5%
5	2 8	random	100	5	5	8	2	5%	5%
6	2 8	random	100	5	5	2 5 8	2 5 8	20%	5%
7	2 8	random	100	5	5	2 5 8	2 5 8	5%	20%
8	2 8	random	100	5	1	2 5 8	2 5 8	5%	5%

Table 7 shows the steady-state reconstruction NRMSEs for DOF7 by using different schemes in eight simulation cases. The NRMSEs for the displacement, velocity, and acceleration estimations at this unobserved DOF are listed. The comparison shows that the proposed MRKF algorithm with RTS smoothing (Scheme 6) achieves satisfactory accuracies in various cases; it is constantly better than the traditional down-sampled single rate (low) method (Scheme 3). For displacement reconstruction, the proposed method (Scheme 6) has comparable performance with the single rate (high) method (Scheme 4). Comparing Cases 1 and 2 indicates when the displacement sampling frequency is much lower than that of acceleration, the traditional down-sampling data fusion method could be problematic because most acceleration data are disregarded. Cases 3 to 5 verify the good performance of the proposed MRKF+RTS algorithm under various excitation conditions. In real SHM applications, the sensor noises may be high, and the structural model may be inaccurate. To facilitate the applications in real practice, Cases 6 and 7 are designed to examine the influences of measurement and system noise levels. The proposed MRKF algorithm is quite robust even under relatively high noise levels. In Case 8, c_{RTS} is reduced to 1, and RTS smoothing is conducted more frequently. Compared with the baseline Case 1, Case 8 has a faster computing speed and smaller time delay. The algorithm can be regarded as nearly online. However, the state estimation error is increased slightly compared with Case 1. The selection of the RTS interval c_{RTS} should be determined according to specific requirements in consideration of a tradeoff between computational real-timing and accuracies. Through this parametric analysis, the robustness and superiority of the proposed algorithm are well verified.

Table 7

Steady-state NRMSE for DOF7 obtained by different schemes under eight simulation cases

Reconstructed response	Sensing scheme	NRMSE for DOF 7 (%)							
		Case 1	Case 2	Case 3	Case 4	Case 5	Case 6	Case 7	Case 8
dis	1 Acc only	3.50	3.50	7.32	1.90	3.91	5.16	7.69	3.50
	2 Dis only	32.7	28.4	25.8	20.1	70.8	63.0	23.7	32.7
	3 Single rate (low)	24.8	2.45	16.9	13.4	68.0	60.8	5.06	24.8
	4 Single rate (high)	0.59	0.59	0.73	0.35	2.00	1.29	0.74	0.59
	5 MRKF	2.04	0.74	4.02	1.16	3.11	3.23	4.36	2.04
	6 MRKF+RTS	0.97	0.57	1.55	0.58	2.26	2.25	1.74	1.07
vel	1 Acc only	3.14	3.14	5.07	2.65	3.47	4.26	6.65	3.14
	2 Dis only	33.5	21.9	36.7	27.6	40.1	48.2	22.7	33.5
	3 Single rate (low)	29.5	6.53	34.5	22.4	37.2	46.8	17.3	29.5
	4 Single rate (high)	2.34	2.34	3.20	2.01	2.88	3.24	4.46	2.34

	5	MRKF	2.84	2.43	4.25	2.42	3.29	3.65	5.94	2.84
	6	MRKF+RTS	2.12	2.02	2.79	1.83	2.52	2.93	4.35	2.33
acc	1	Acc only	3.58	3.58	3.75	3.77	4.37	4.76	5.95	3.58
	2	Dis only	21.9	17.0	19.5	20.7	17.4	16.8	20.1	21.9
	3	Single rate (low)	18.6	5.82	14.1	19.5	32.8	16.6	7.54	18.6
	4	Single rate (high)	3.06	3.06	2.86	3.24	3.92	4.63	4.12	3.06
	5	MRKF	3.57	3.18	3.59	3.76	4.35	4.78	5.76	3.57
	6	MRKF+RTS	2.67	2.78	2.60	2.78	3.06	4.01	4.03	2.89

4. Experimental validation

4.1 Experimental setup

A steel cantilever beam was tested in the laboratory to examine the effectiveness of the proposed algorithm. As shown in Fig. 7, the cantilever beam with a cross-section of 50 mm × 3.14 mm was installed on a shake table. The total height of the beam was 1,180 mm and was equally divided into eight elements in its numerical model.

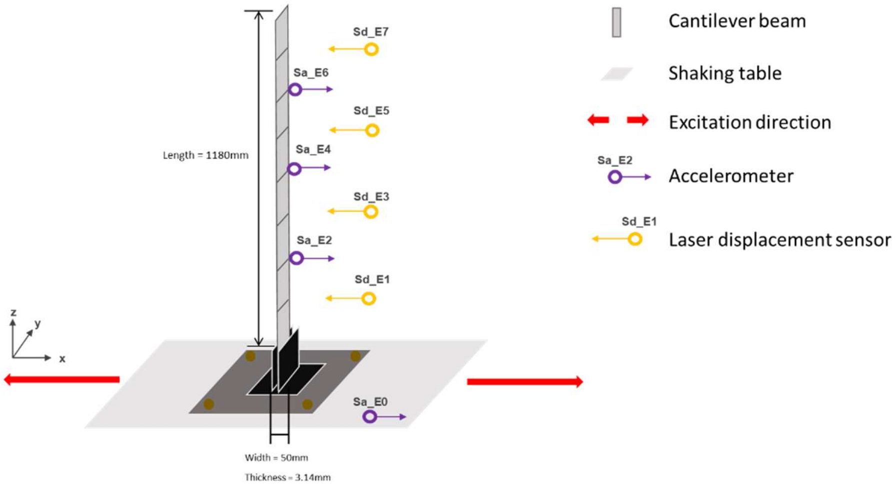

Fig. 7. Layout of the sensors in the laboratory test

The APS420 long-stroke shaker generated the ground excitation. Acceleration responses were measured by three accelerometers (Type 4382, Brüel & Kjær, Denmark), installed at DOF2, DOF4, and DOF6, and denoted as Sa_E2, Sa_E4, and Sa_E6 in Fig. 7. The beam displacement was recorded by an iPhone 11 placed in front of the beam. Markers were attached to the locations where beam displacements were to be extracted. The displacement was extracted from the recorded video by using the Kanade-Lucas-Tomasi (KLT) tracking algorithm. Four laser displacement meters (IL-300, Keyence Corporation of America, USA) were also installed to examine the accuracy of the KLT tracking algorithm. The iPhone 11 and the laser displacement meters recorded absolute displacements, which include the shake table displacement. The excitation time history generated by the shake table was recorded by an accelerometer Sa_E0. The data acquisition (DAQ) system is KYOWA EDX-100A, and the sampling frequency for accelerometers and laser displacement sensors was set to 1000 Hz. Fig. 8 shows the photos of the experimental setup in the laboratory.

The natural frequencies of the tested beam were identified using the stochastic subspace identification (SSI) technique. The measured first three frequencies were 1.706 Hz, 10.834 Hz, and 30.260 Hz, respectively. The model updating was conducted to match the measured results. The steel density was assumed as 7850 kg/m^3, and Young's modulus was 210 GPa. The damping ratios for all modes were assumed as 2% in the calculation

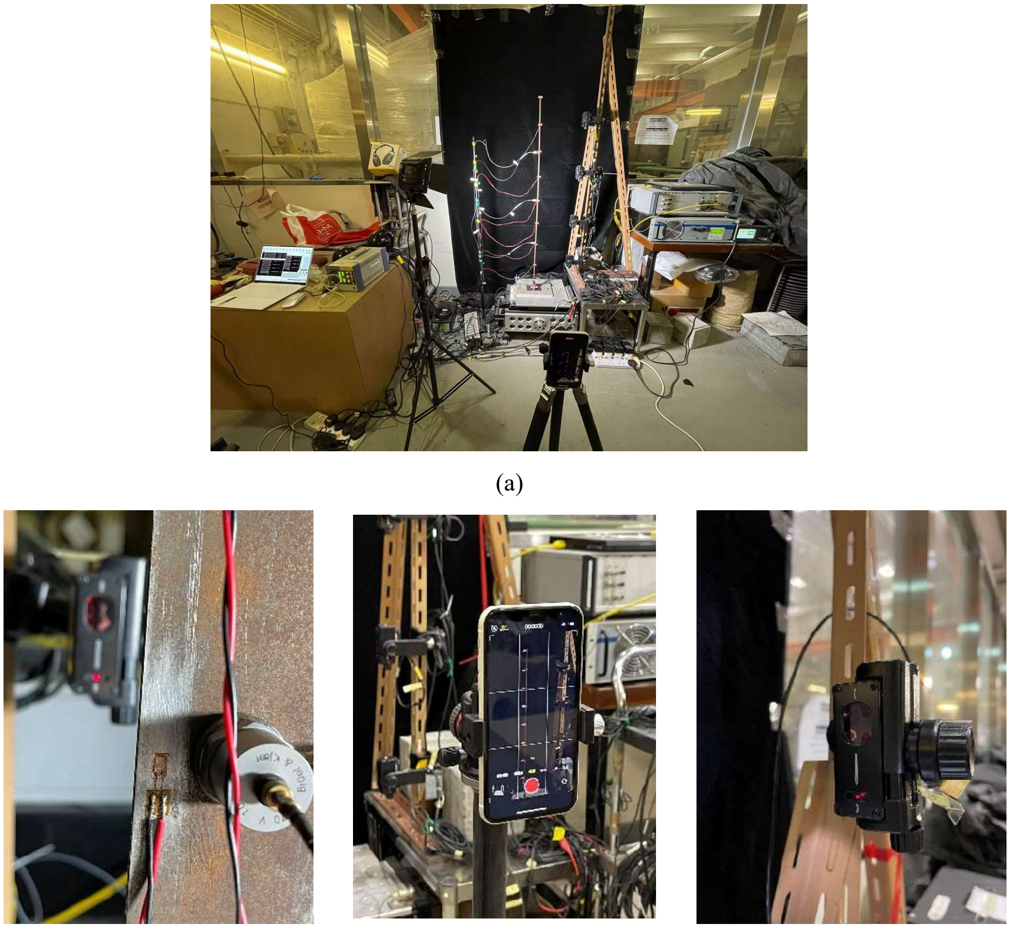

(a)

(b) (c) (d)

Fig. 8. Laboratory experimental setup: (a) whole picture, (b) accelerometer, (c) iPhone11, and (d) laser displacement sensor

4.2 Camera tracking results

Although a professional high-speed camera can provide accurate motion tracking at high frame rates, its application is hindered by the exorbitant price. Motion tracking by using consumer-grade cameras is quite propitious in SHM applications. The KLT tracking algorithm is one of the target-free computer-vision methods. It was successfully applied to the motion tracking of one six-story shear frame by Yoon et al. in 2016 [41]. Fig. 9 shows the vision-based displacement measurement procedure in this experimental test. An iPhone 11 recorded the structure motions by filming videos, and the available frame rates were 30 and 60 fps. Regions of Interest (ROIs) were selected in the first frame and were automatically tracked in the following video frames. The ROIs were equivalent to the sensor locations in traditional SHM. Although the markers are not really required by the KLT method, they were still used in this test to improve the tracking quality because the beam thickness was too thin. Once the ROIs are selected for the first frame, the KLT algorithm can track the point pixel locations for the entire duration of the video. By calculating the pixel distance between two points with known physical lengths, the pixel-to-mm convention was obtained. The structural displacement could be obtained thereafter.

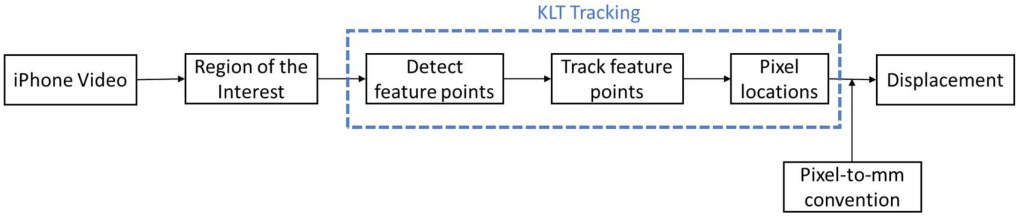

Fig. 9. Vision-based displacement measurement procedure using KLT tracking

As shown in Fig. 8, the light absorbing background was placed behind the test beam, and the markers were placed on each beam node and the shake table. The pixel-to-mm coefficient was determined as 0.37 in this test, i.e., one pixel in the video frame is 0.37 mm displacement in physical coordinate. Fig. 10 compares the displacements measured by the laser displacement meters and iPhone 11. The results obtained by the iPhone agree well with the laser displacement meter measurements. The RMSEs for DOF1, DOF3, DOF5, and DOF7 are only 0.245 mm, 0.477

mm, 0.514 mm, and 0.540 mm, respectively. More importantly, one iPhone model could track structural motions at many points; whereas one laser displacement meter could only measure one single point, and it usually has a narrow operating distance range. The tracking results in this experiment demonstrate the great potential for deploying the consumer-grade camera for displacement measurements in SHM applications.

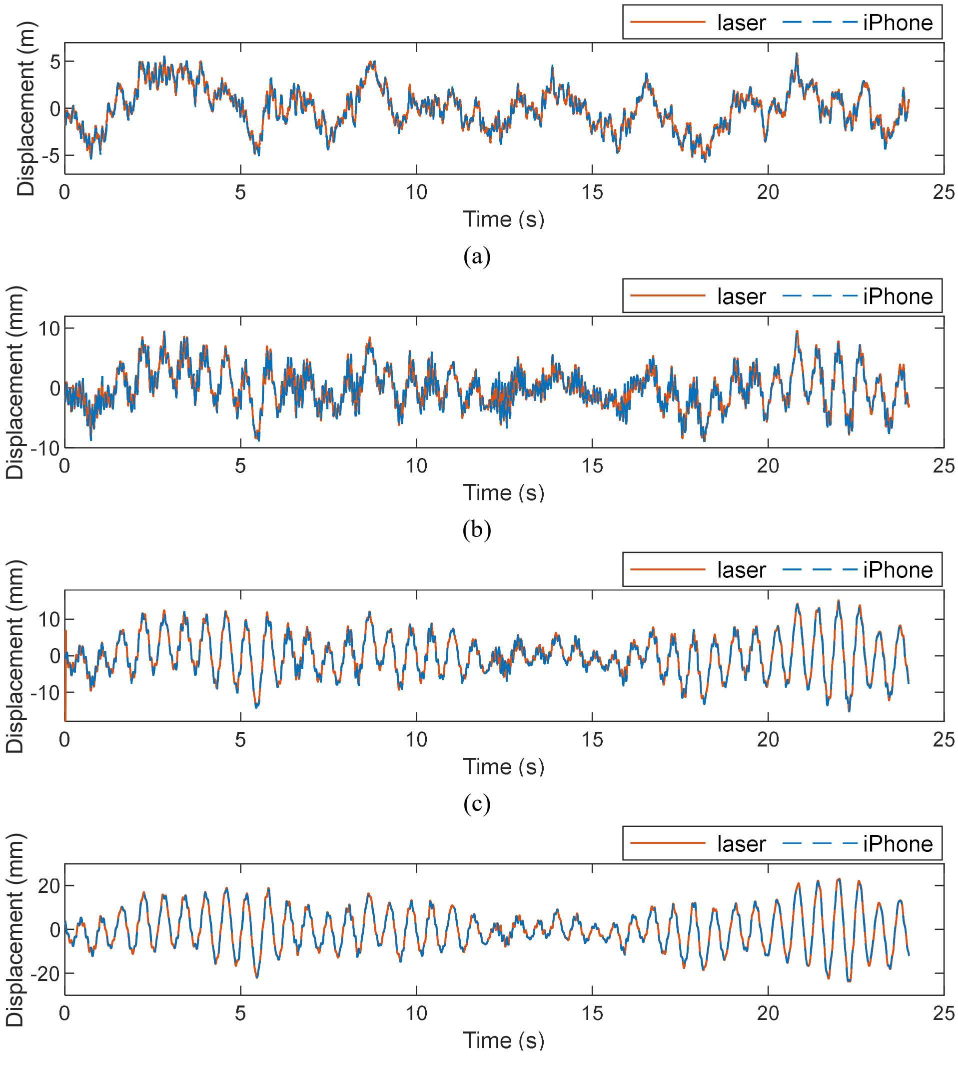

(a)

(b)

(c)

(d)

Fig. 10. Compare displacement measured by iPhone and laser displacement in laboratory test: (a) DOF1, (b) DOF3, (c) DOF5, and (d) DOF7

4.3 Response reconstruction results

A random ground motion with a frequency range of 0 Hz to 50 Hz and amplitude of 8 m/s^2 was applied to the cantilever beam. The frequency was selected to cover the first three natural frequencies of the test beam. Out of the three installed accelerometers, only Sa_E2 and Sa_E4 observations were used to reconstruct structural responses. The acceleration recorded by Sa_E6 was used for the comparison with the reconstructed responses. Displacement at all eight DOFs could be extracted from the recorded videos. In this experimental test, only two displacements at DOF3 and DOF5 were included in the observation vector. Displacement measurements at other locations were used to verify filter accuracies. The standard deviation of measurement noise $\boldsymbol{\upsilon}_k$ was estimated to be around 10% of the standard deviation of the measured responses. The variance of system noise was set as the square of 5% of the standard deviation of the state vector. The sampling frequency of the accelerometers and laser displacement meters was set as 1000 Hz. The video frame rate of the iPhone11 camera was 60 fps. Considering the proposed MRKF algorithm only applies to the case where the sampling frequency of the acceleration is integer multiples of the displacement, the camera-tracked displacements were down-sampled from 60 fps to 20 fps for calculation.

Fig. 11 presents the reconstructed displacement time histories at verification DOFs. The same six different data fusion schemes were adopted for a better illustration of the algorithm performance and consistency with the numerical simulation. The reconstructed displacements are compared with the KLT tracking results. Displacement estimation by using displacement sensors (Scheme 2) and single rate low (Scheme 3) failed to produce satisfactory results, which is consistent with the conclusion reached in the numerical simulation. Response reconstruction by using data sampled at low frequencies will lose the ability to capture higher-order structural vibration modes. Given that high-frequency displacement data were unavailable from the vision-based tracking, displacements recorded by laser displacement meters were used in the single rate (high) data fusion based on 1000 Hz acceleration and displacement measurements (Scheme 4). Fig. 11 shows that the proposed MRKF algorithm with RTS smoothing process yields competitive results with data fusion by high single rate observations. The estimations agree fairly with the measured sensor data. If only acceleration observation is used in the observation, the reconstructed displacements have larger errors than the MRKF results. Table 8 presents the NRMSEs for the reconstructed displacements in the laboratory test. The MRKF errors can be further reduced by approximately 1% - 25% if the RTS smoothing procedure is applied. After the smoothing, the reconstruction errors in

Scheme 6 were reduced by around 30%-80% compared with estimation using acceleration only (Scheme 1) and by over 90% compared with traditional down-sampling single rate data fusion (Scheme 3).

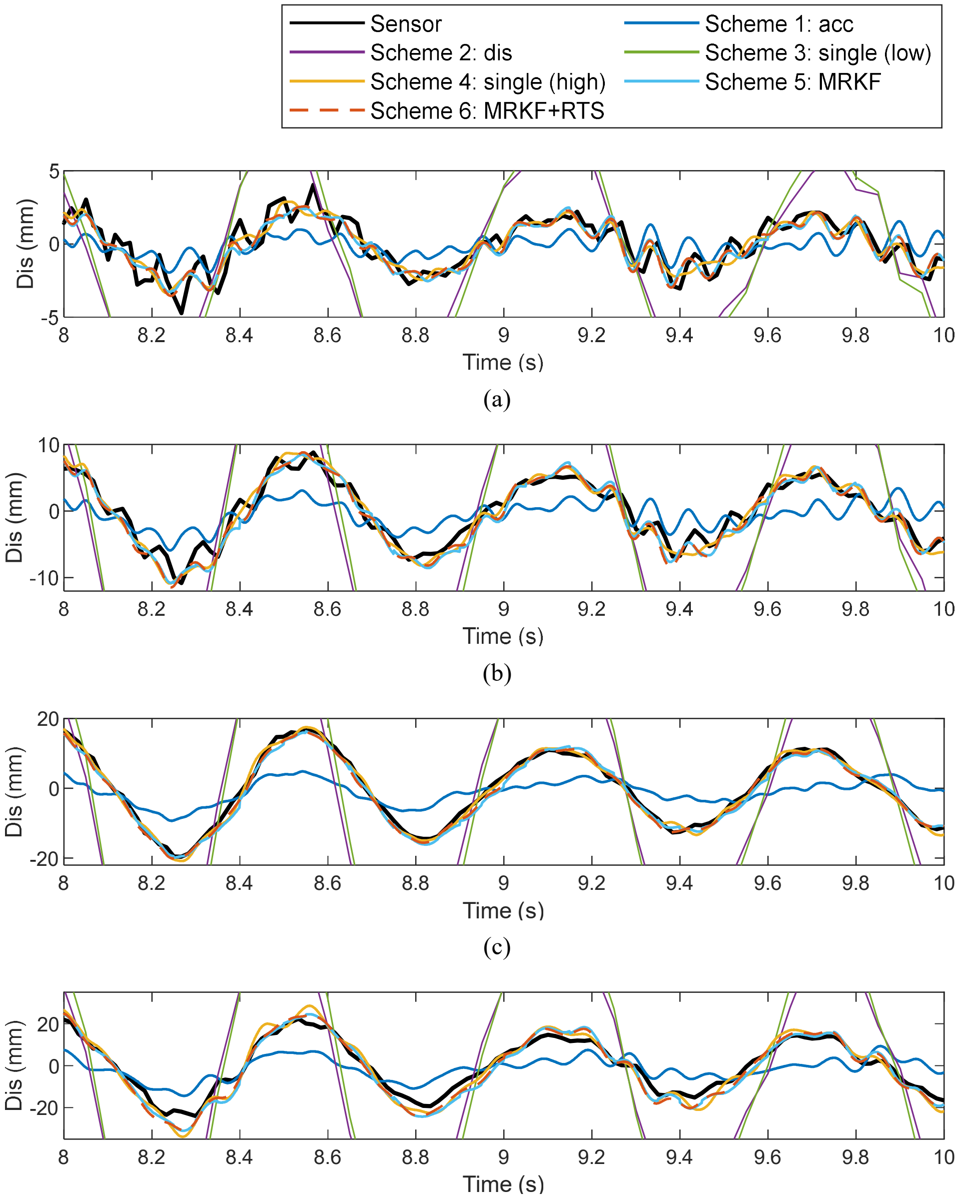

(a)

(b)

(c)

(d)

Fig. 11. Displacement estimations at verification DOFs in laboratory test (a) DOF2, (b) DOF4, (c) DOF6, and (d) DOF8

Fig. 12 compares the reconstructed acceleration and the accelerometer measurement at DOF6. Except for Schemes 2 and 3, all other schemes achieve similar performance. A similar conclusion can be reached from the data presented in Table 9. If only structural accelerations are required to be estimated under known input, response reconstruction by using acceleration only will provide acceptable estimations. However, if displacement and velocity responses are of interest as well, data fusion shall be conducted to obtain better structural state estimations.

Table 8

Steady-state NRMSE for displacement obtained by using different schemes for the tested beam

Scheme		NRMSE for displacement (%)							
		DOF1	DOF2	DOF3	DOF4	DOF5	DOF6	DOF7	DOF8
1	Acc only	16.85	16.63	16.32	16.77	16.30	16.99	17.86	18.72
2	Dis only	37.34	41.58	46.52	58.54	54.23	58.45	60.54	72.78
3	Single rate (low)	39.41	43.92	49.43	62.66	57.80	62.33	64.53	78.08
4	Single rate (high)*	10.41	8.797	6.864	5.981	3.392	2.605	3.144	6.337
5	MRKF	11.62	10.03	8.152	7.154	4.228	3.495	4.401	6.983
6	MRKF+RTS	11.48	10.01	8.047	6.811	4.205	2.958	3.285	6.149

*Laser displacement sensor is used given that high frequency camera reading is unavailable.

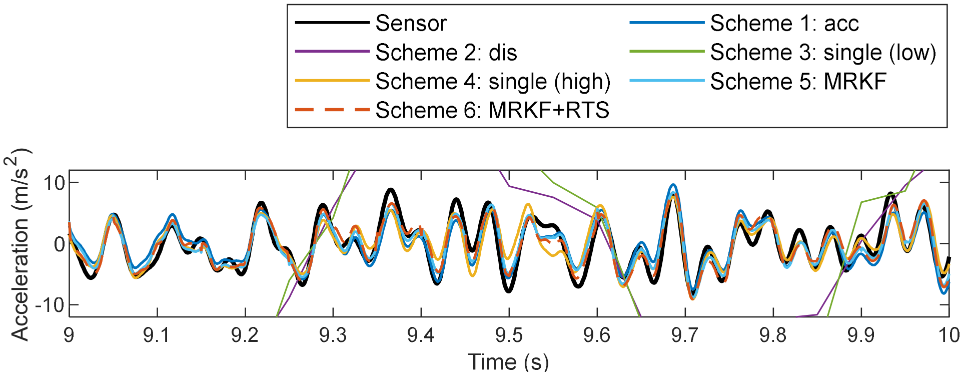

Fig. 12. Acceleration time history at DOF6 in laboratory test

Table 9

Steady-state NRMSE for acceleration obtained by using different schemes in the test

Scheme		NRMSE for acceleration (%)		
		DOF2	DOF4	DOF6
1	Acc only	0.136	0.096	9.352
2	Dis only	37.90	37.05	45.58
3	Single rate (low)	0.972	1.024	56.47
4	Single rate (high)*	0.136	0.096	9.685
5	MRKF	0.592	0.463	11.89
6	MRKF+RTS	0.163	0.115	10.18

*Laser displacement sensor is used because high-frequency camera reading is unavailable.

5. Conclusions

A novel MRKF data fusion algorithm combined with an RTS smoothing technique for structural dynamic response reconstruction, which enables the direct fusion of signals sampled at different frequencies, is presented in this paper for the first time. The proposed method adopts two sets of observation equations for the measurements. The measurement update using displacement and acceleration will be conducted only when the displacement data are available; otherwise, the acceleration observation equation will be adopted. The RTS smoothing procedure is further applied to enhance the estimation precisions. The proposed algorithm surmounts the obstacle to deploying low-cost consumer-grade cameras in SHM applications. Through the numerical simulations and laboratory tests of different structures in various scenarios, the robustness and superiority of the proposed MRKF algorithm are successfully verified. Below are the major conclusions of this paper:

1. The proposed MRKF algorithm is the first response reconstruction technique for an MDOF structural system that considers the fusion of multi-type sensor data sampling at different rates.

2. The partially observed system is allowed, and the collocated sensor monitoring requirement is relaxed. Unobserved responses will be estimated through the proposed MRKF iterations.

3. Compared with traditional KF-based algorithms, the proposed algorithm is relatively robust and insensitive to noises. Satisfactory state estimations could still be obtained even with high measurement and system noises.

4. The RTS smoothing process leads to time delay to some extent in response reconstruction. When the RTS interval c_{RTS} is small, the algorithm is nearly online but will produce larger estimation errors. The selection of the RTS interval c_{RTS} should be determined according to specific requirements by considering a tradeoff between computational real-timing and accuracies.

5. MRKF solves the inherent problem of the low sampling rate of displacement monitoring by consumer-grade cameras. Through the proposed MRKF iterations and RTS smoothing, the state estimation results can be comparable to those obtained by high-frequency acceleration and displacement measurements. This finding can potentially reduce the SHM sensing system

budget by avoiding using an expensive high-speed camera.

The presented findings illustrate the superiority and robustness of the proposed algorithm in various scenarios. However, the current algorithm only applies when the acceleration sampling frequency is integer multiples of the displacement sampling frequency. The excitation should also be measured. And the current algorithm is only applicable to linear systems within elastic range. Future studies will be carried out to extend the proposed algorithm to more generic cases and improve filter practicability.

Declaration of Competing Interest

The authors declare that they have no known competing financial interests or personal relationships that could have appeared to influence the work reported in this paper.

Acknowledgement

This research was supported by the Research Grants Council of Hong Kong through Theme-based Research Scheme (T22-502/18-R), Research Impact Fund (PolyU R5020-18), and General Research Fund (15213122), the Hong Kong Branch of the National Rail Transit Electrification and Automation Engineering Technology Research Center (No. K-BBY1), and The Hong Kong Polytechnic University (ZE2L, ZVX6).

References

1. Ni YQ, Wang YW and Zhang C. A Bayesian approach for condition assessment and damage alarm of bridge expansion joints using long-term structural health monitoring data. *Eng Struct* 2020; 212: 110520.
2. Ni YQ, Xia Y, Liao WY and Ko JM. Technology innovation in developing the structural health monitoring system for Guangzhou New TV Tower. *Struct Control Health Monit* 2009; 16(1): 73-98.
3. Xia Y, Zhang P, Ni YQ and Zhu HP. Deformation monitoring of a super-tall structure using real-time strain data. *Eng Struct* 2014; 67: 29-38.
4. Feng D and Feng MQ. Computer vision for SHM of civil infrastructure: From dynamic response measurement to damage detection–A review. *Eng Struct* 2018; 156: 105-117.
5. Moyo P, Brownjohn JMW, Suresh R and Tjin SC Development of fiber Bragg grating sensors for monitoring civil infrastructure. *Eng Struct* 2005; 27: 1828-1834.
6. Kammer DC. Estimation of structural response using remote sensor locations, *J Guid Control Dyn* 1997; 20(3): 501-508.
7. Law SS, Li J and Ding Y. Structural response reconstruction with transmissibility concept in

frequency domain. *Mech Syst Signal Process* 2011; 25(3): 952-968.

8. He J, Guan X and Liu Y. Structural response reconstruction based on empirical mode decomposition in time domain. *Mech Syst Signal Process* 2012; 28: 348-366.
9. Limongelli MP. Optimal location of sensors for reconstruction of seismic responses through spline function interpolation. *Earthq Eng Struct Dyn* 2003; 32(7): 1055-1074.
10. Kullaa J. Bayesian virtual sensing in structural dynamics. *Mech Syst Signal Process* 2019; 115: 497-513.
11. Saltari F, Dessi D, and Mastroddi F. Mechanical systems virtual sensing by proportional observer and multi-resolution analysis. *Mech Syst Signal Process* 2021; 146: 107003.
12. Kalman RE. A new approach to linear filtering and prediction problems. 1960.
13. Zhu S, Zhang XH, Xu YL and Zhan S. Multi-type sensor placement for multi-scale response reconstruction. *Adv Struct Eng* 2013; 16(10): 1779-1797.
14. Xu YL, Zhang XH, Zhu S and Zhan S. Multi-type sensor placement and response reconstruction for structural health monitoring of long-span suspension bridges. *Sci Bull* 2016; 61(4): 313-329.
15. Zhang XH, Zhu Z, Yuan GK and Zhu S. Adaptive Mode Selection Integrating Kalman Filter for Dynamic Response Reconstruction. *J Sound Vib* 2021; 515:116497.

16 Lei Y, Zhou H and Lai ZL. A computationally efficient algorithm for real-time tracking the abrupt stiffness degradations of structural elements. *COMPUT-AIDED CIV INF* 2016; 31(6): 465-480.

17. Lei Y, Lu J and Huang, J. Synthesize identification and control for smart structures with time-varying parameters under unknown earthquake excitation. *Struct Control Health Monit* 2020; 27(4): e2512.
18. Ebrahimzadeh Hassanabadi M, Heidarpour A, Eftekhar Azam S, and Arashpour M. A Bayesian smoothing for input-state estimation of structural systems. *COMPUT-AIDED CIV INF* 2022; 37(3), 317-334.
19. Hwang J, Kwon D, and Kareem A. A modal-based Kalman filtering framework for mode extraction and decomposition of damped structures. *COMPUT-AIDED CIV INF* 2022; 1-16.
20. Ebrahimzadeh Hassanabadi M, Liu Z, Eftekhar Azam S, and Dias-da-Costa, D. A linear Bayesian filter for input and state estimation of structural systems. *COMPUT-AIDED CIV INF* 2023; 1-18.
21. Gillijns S and De Moor B. Unbiased minimum-variance input and state estimation for linear discrete-time systems. *Automatica* 2007; 43(1):111-116.
22. Gillijns S and De Moor B. Unbiased minimum-variance input and state estimation for linear discrete-time systems with direct feedthrough. *Automatica* 2007; 43(5): 934-937.
23. Zhang XH, Xu YL, Zhu S and Zhan S. Dual-type sensor placement for multi-scale response reconstruction. *Mechatronics* 2014; 24(4): 376-384.
24. Zhang XH, Zhu S, Xu YL and Homg XJ. Integrated optimal placement of displacement transducers and strain gauges for better estimation of structural response. *Int J Struct Stab Dyn* 2011; 11(03): 581-602.
25. Zhang CD and Xu YL. Optimal multi-type sensor placement for response and excitation reconstruction. *J Sound Vib* 2016; 360: 112-128.
26. Li T, Pan Y, Tong K, Ventura CE and de Silva CW. A multi-scale attention neural network for sensor location selection and nonlinear structural seismic response prediction. *Comput Struct*

2021; 248: 106507.

27. Kaloop MR, Elbeltagi E, Hu JW and Elrefai A. Recent advances of structures monitoring and evaluation using GPS-time series monitoring systems: A review. *ISPRS Int J Geoinf* 2017; 6(12): 382.
28. Dong C, Celik O, Catbas F, O'Brien E and Taylor S. Structural displacement monitoring using deep learning-based full field optical flow methods. *Struct. Infrastruct. Eng.* 2020; 16(1), 51-71.
29. Xu Y, Zhang J and Brownjohn, J. An accurate and distraction-free vision-based structural displacement measurement method integrating Siamese network based tracker and correlation-based template matching. *Measurement* 2021; 179, 109506.
30. Dong C and Catbas, F. N. A non-target structural displacement measurement method using advanced feature matching strategy. *Adv. Struct* 2019; 22(16), 3461-3472.
31. Smyth A and Wu M. Multi-rate Kalman filtering for the data fusion of displacement and acceleration response measurements in dynamic system monitoring. *Mech Syst Signal Process* 2007; 21(2): 706-723.
32. Chang CC and Xiao X. An integrated visual-inertial technique for structural displacement and velocity measurement. *Smart Struct Syst* 2010; 6(9): 1025-1039.
33. Zhu H, Gao K, Xia Y, Gao F, Weng S, Sun Y and Hu Q. Multi-rate data fusion for dynamic displacement measurement of beam-like supertall structures using acceleration and strain sensors. *Struct Health Monit* 2020; 19(2): 520-536.
34. Kim J, Kim K and Sohn H. Autonomous dynamic displacement estimation from data fusion of acceleration and intermittent displacement measurements. *Mech Syst Signal Process* 2014; 42(1-2): 194-205.
35. Kim K, Choi J, Koo G and Sohn H. Dynamic displacement estimation by fusing biased high-sampling rate acceleration and low-sampling rate displacement measurements using two-stage Kalman estimator. *Smart Struct Syst* 2016; 17(4): 647-667.
36. Zheng Z, Qiu H, Wang Z, Luo S and Lei Y. Data fusion based multi-rate Kalman filtering with unknown input for on-line estimation of dynamic displacements. *Measurement* 2019; 131: 211-218.
37. Ma Z, Choi J and Sohn H. Real-time structural displacement estimation by fusing asynchronous acceleration and computer vision measurements. *COMPUT-AIDED CIV INF* 2022; 37(6), 688-703.
38. Rauch HE, Tung F Striebel CT. Maximum likelihood estimates of linear dynamic systems. *AIAA J* 1965; 3(8): 1445-1450.
39. De Callafon RA, Moaveni B, Conte JP, He X and Udd E. General realization algorithm for modal identification of linear dynamic systems. *J Eng Mech* 2008; 134(9): 712-722.
40. Azam SR, Chatzi E and Papadimitriou C. A dual Kalman filter approach for state estimation via output-only acceleration measurements. *Mech Syst Signal Process* 2015; 60: 866-886.
41. Yoon H, Elanwar H, Choi H, Golparvar Fard M and Spencer Jr BF. Target-free approach for vision-based structural system identification using consumer-grade cameras. *Struct Control Health Monit* 2016; 23(12): 1405-1416.